



## Experimental-computational study of fibrous particle transport and deposition in a bifurcating lung model



Xiaole Chen<sup>a</sup>, Wenqi Zhong<sup>a,\*</sup>, Josin Tom<sup>b</sup>, Clement Kleinstreuer<sup>b,c</sup>, Yu Feng<sup>d</sup>, Xiaopu He<sup>e</sup>

<sup>a</sup> Key Laboratory of Energy Thermal Conversion and Control of the Ministry of Education, School of Energy and Environment, Southeast University, Nanjing 210096, China

<sup>b</sup> Department of Mechanical and Aerospace Engineering, North Carolina State University, Raleigh, NC 27695, USA

<sup>c</sup> Department of Biomedical Engineering, North Carolina State University, Raleigh, NC 27695, USA

<sup>d</sup> School of Chemical Engineering, Oklahoma State University, Stillwater, OK 74078, USA

<sup>e</sup> First Affiliated Hospital of Nanjing Medical University, Nanjing 210029, China

### ARTICLE INFO

#### Article history:

Received 3 August 2015

Received in revised form

26 December 2015

Accepted 11 February 2016

Available online 8 June 2016

#### Keywords:

Lung aerosol dynamics

Image-processing method

Fiber deposition data

Computer simulations

Deposited fiber orientations

### ABSTRACT

Experiments carried out using a lung model with a single horizontal bifurcation under different steady inhalation conditions explored the orientation of depositing carbon fibers, and particle deposition fractions. The orientations of deposited fibers were obtained from micrographs. Specifically, the effects of the sedimentation parameter ( $\gamma$ ), fiber length, and flow rate on orientations were analyzed. Our results indicate that gravitational effect on deposition cannot be neglected for  $0.0228 < \gamma < 0.247$ . The absolute orientation angle of depositing fibers decreased linearly with increasing  $\gamma$  for values  $0.0228 < \gamma < 0.15$ . Correspondence between Stokes numbers and  $\gamma$  suggests these characteristics can be used to estimate fiber deposition in the lower airways. Computer simulations with sphere-equivalent diameter models for the fibers explored deposition efficiency vs. Stokes number. Using the volume-equivalent diameter model, our experimental data for the horizontal bifurcation were replicated. Results for particle deposition using a lung model with a vertical bifurcation indicate that body position also affects deposition.

© 2016 Chinese Society of Particuology and Institute of Process Engineering, Chinese Academy of Sciences. Published by Elsevier B.V. All rights reserved.

### Introduction

Man-made inhalable fibers may cause detrimental health effects, as in the case of asbestos, as well as carbon and vitreous fibers (Blake et al., 1998; Cavallo et al., 2004; Champion & Mitragotri, 2006; Hodgson & Darnton, 2000; Kulkarni, Baron, & Willeke, 2011; LeMasters et al., 2003; Marsh et al., 2001; Mossman & Churg, 1998). Alternatively, they can be used for treatment, as in the case of therapeutic drug particles (Simone, Dziubla, & Muzykantov, 2008). Thus, computational and experimental analyses of the transport and deposition of non-spherical aerosols in models of the human lung are of great interest. For example, Myojo (1987) experimentally examined fiber deposition in a single-bifurcation airway, and qualitatively stated that the deposited fibers traveled parallel to the carrier–fluid flow. Furthermore, Myojo (1990) investigated the effects of fiber length and diameter on fiber deposition. Myojo and Takaya (2001) proposed an empirical

correlation to estimate the deposition fraction (DF) of fibrous particles linked to impaction and interception. Sussman, Cohen, and Lippmann (1991) studied the effects of asbestos fiber length and flow rates on deposition efficiency (DE) in a tracheobronchial airway. Marijnissen, Zeckendorf, Lemkowitz, and Bibo (1991) analyzed the deposition of nylon fibers in an upper airway, and concluded that the deposition hot spot of nylon fibers at the carina is similar to that of spherical particles. Su and Cheng (2005) investigated fiber deposition in the human nasal airways at different flow rates. Their results indicated that the dominant mechanism was impaction, and that fibrous particles could pass through the nasal cavity more easily than spherical ones. Su and Cheng (2006) emphasized the effect of impaction in experiments on deposition of fibers in an airway replica, comprising an oral cavity, pharynx, larynx, and pulmonary bifurcations. Further experimental observations (Zhou, Su, & Cheng, 2007) showed that fibers could penetrate the upper respiratory airways and enter lower lung regions more easily than spherical particles having the same volume. Wang, Hopke, Ahmadi, Cheng, and Baron (2008) analyzed the influences of fiber length, flow rate, and airway geometry on particle deposition in nasal cavities. Examples of recent numerical analyses of fiber deposition in

\* Corresponding author. Tel.: +86 25 83794744; fax: +86 25 83795508.  
E-mail address: [wqzhong@seu.edu.cn](mailto:wqzhong@seu.edu.cn) (W. Zhong).

## Nomenclature

$d_{ae}$	fiber's aerodynamic equivalent diameter
$d_p$	diameter of fibrous particle
$d_{ve}$	fiber's volume equivalent diameter
$d^*$	dimensionless particle diameter
$D$	inlet tube diameter
DF	deposition fraction
$Fr$	Froude number
$g$	gravitational acceleration
$m_{deposit}$	particle mass deposited on the inner airway surfaces
$m_{exit}$	particle mass which had exited the airway model
$L$	length of the airway tube
$l_p$	length of fibrous particle
$St$	Stokes number
$U$	mean air velocity at the inlet
$v^*$	dimensionless terminal velocity
$v_{setting}$	settling/terminal velocity of the particle

## Greek letters

$\beta$	aspect ratio of fiber
$\gamma$	sedimentation parameter
$\kappa$	dynamic shape factor
$\kappa_{\parallel}$	dynamic shape factors of the fibers oriented parallel to the flow
$\kappa_{\perp}$	dynamic shape factors of the fibers oriented perpendicular to the flow
$\theta$	orientation angle of deposited fiber
$ \theta $	absolute value of the orientation angle
$\langle  \theta  \rangle$	average of the absolute orientation angle
$\mu$	dynamic viscosity of air
$\rho_f$	density of fluid
$\rho_p$	density of fiber
$\rho_0$	density of water
$\varphi$	inclination angle measured relative to the horizontal
$\phi$	particle sphericity

realistic nasal cavities include simulations by [Inthavong, Wen, Tian, and Tu \(2008\)](#) and [Shanley, Ahmadi, Hopke, and Cheng \(2009\)](#); the latter group compared fibrous particle DEs to those of spheres. [Tian and Ahmadi \(2013\)](#) analyzed the flow field, fiber trajectory, and DE in an asymmetric, generation G0–G3 lung bifurcation model. [Feng and Kleinstreuer \(2013\)](#) investigated ellipsoidal particle transport in Poiseuille flow, which resulted in a revised Stokes-equivalent-diameter for ellipsoidal particles. They compared their simulations to measured data sets for ellipsoidal particles to predict the DEs in subject-specific airways from the oral cavity to a G3 lung model. [Kleinstreuer and Feng \(2013\)](#) reviewed spherical and non-spherical fluid-particle dynamics, and discussed different numerical methods for non-spherical particle simulations.

Nevertheless, the behavior of fibrous particles in deeper lung regions is still unclear, especially when the effect of gravitational sedimentation on deposition becomes a factor. For example, [Sakai, Watanabe, Sera, Yokota, and Tanaka \(2015\)](#) carried out deposition experiments in nasal cavities with large particles (i.e., lycopodium powder, with an average diameter of  $32\ \mu\text{m}$  and density of  $1.05 \times 10^3\ \text{kg/m}^3$ ), and showed that DE is about 15–25% higher than the experimental correlation proposed by [Kelly, Asgharian, Kimbell, and Wong \(2004\)](#) for 1- to  $10\text{-}\mu\text{m}$ -sized particles undergoing sedimentation. [Kleinstreuer, Zhang, and Kim \(2007\)](#) simulated spherical micron-sized particle deposition in a G6–G9 airway, taking into account inertial impaction and sedimentation. Their results also showed that gravitational sedimentation becomes

locally significant in some lung airways, influencing deposition patterns as well as DEs, especially under slow inhalation conditions. [Hofmann, Balásházy, and Koblinger \(1995\)](#) simulated spherical particle deposition in a single-bifurcation G15–G16 airway under different gravity angles, using a Monte Carlo method. The simulations showed that deposition was greatly affected by the angle between the parent tube axis and the gravitational vector; horizontally placed bifurcations yielded the highest DEs. Sedimentation is more complicated for fibers than for spherical particles, because their motion is influenced by their orientation in the fluid flow field. For example, the settling velocity of a high-aspect-ratio fiber released parallel to the gravitational vector is about twice that attained when descending perpendicular to gravity ([Herzhaft & Guazzelli, 1999](#)).

The goal of our study is to investigate fiber deposition in a bifurcating lung model to obtain quantitative data on the orientation of fibrous particles during transport and deposition. Using steady air-fiber flow in a single-bifurcation airway model, following the geometry of [Weibel \(1963\)](#), the DEs of fibrous particles were acquired under different flow rates. Images of local particle deposition were captured using a microscope and analyzed to obtain fiber orientations. Stokes number and sedimentation parameters were calculated to evaluate the behavior of these fibrous particles in the lower airway. Our data provide new insights into fiber behavior that can be used for computer modeling of the transport and deposition of fibrous particles with a lung model.

## Method

### Fiber characteristics

Black carbon fibers were used in experiments of this study, provided by Corker, Inc. (Hangzhou, China). Carbon fibers provide a high contrast to the system background, ideal for imaging. The fibers were monodisperse in diameter, but polydisperse in length. Fiber length and diameter distributions shown in [Fig. 1](#) were obtained by measuring fibers ( $N > 200$ ) on SEM images. Their count median diameter (CMD) was  $7.34\ \mu\text{m}$  and the geometric standard deviation of the diameter was 1.07. Their count median length (CML) was  $22.97\ \mu\text{m}$ , and the geometric standard deviation of the length was 1.81. The density of the fiber was  $1780\ \text{kg/m}^3$ .

### Experimental setup

The G0–G1 bifurcating model shown in [Fig. 2](#) was reproduced from Weibel's 23-generation pulmonary airway model ([Weibel, 1963](#)) using a 3D printer (ZBuidner, Zcorp, Burlington, USA). The rectangles in [Fig. 2](#) show the positions selected to observe the orientations of deposited fibers using a microscope. The interval between neighboring observation points was 10 mm. Position 11 (P11) was omitted to facilitate discussion of results for G0 and G1 model sections. Physical parameters of our model are listed in [Table 1](#). The orientation angle  $\theta$  is defined as the angle between the axial directions of the tube and the deposited fiber, as illustrated in [Fig. 2](#). The inner surface of our airway model was coated with a sodium polyacrylate solution to cause fibers to adhere to its surface.

[Fig. 3](#) illustrates the experimental setup of our fiber deposition experiments under steady inhalation conditions. The experimental system consists of a fiber generator, a mixing chamber, the airway model, filter units, two flow meters, and a vacuum pump. Fibers were delivered into the mixing chamber by air from the generator, dispersed in the mixing chamber before moving into the airway model under inspiratory flow. Because image processing was used to identify the lengths of deposited fibers, a differential mobility analyzer was not employed. Fibers were randomly

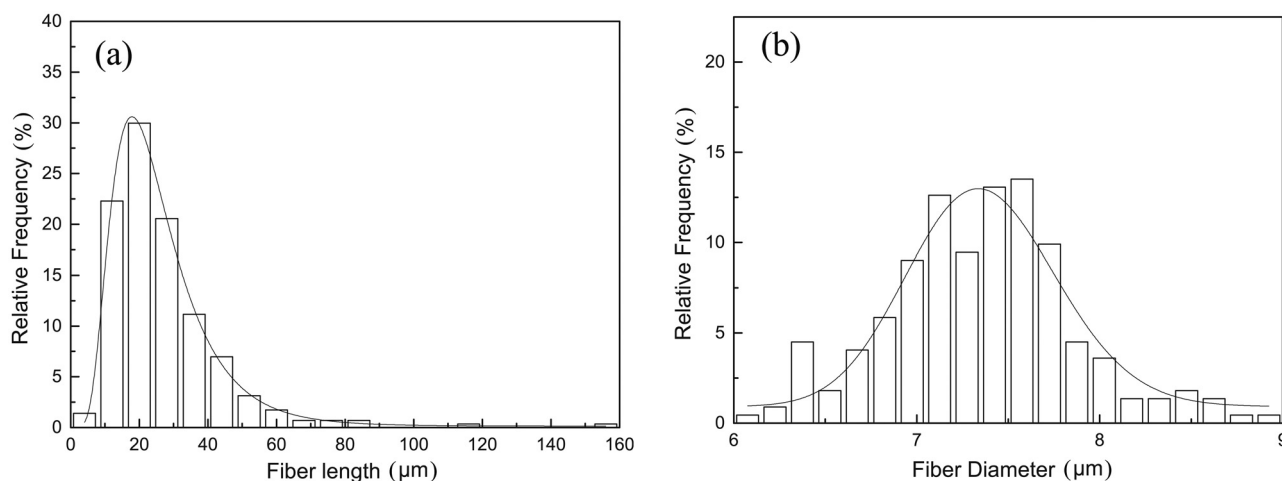


Fig. 1. Fiber length and diameter frequency distributions: (a) length distribution and (b) diameter distribution.

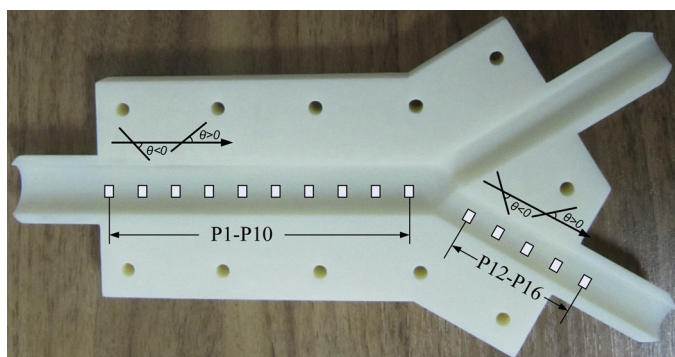


Fig. 2. Top-view of the G0 (P1–P10)–G1 (P12–P16) airway model showing locations of micrograph positions.

Table 1  
Summary of experiment setup parameters.

Parameter	Value
Diameter of G0 (mm)	18
Length of G0 (mm)	120
Diameter of G1 (mm)	12.2
Length of G1 (mm)	48
Fiber's count median diameter ( $\mu\text{m}$ )	7.34
Fiber's count median length ( $\mu\text{m}$ )	22.97
Fiber's aerodynamic equivalent diameter, $d_{ae}$ ( $\mu\text{m}$ )	15.48
Flow rate (L/min)	4, 8, 12, 16
Stokes number	0.0193, 0.0385, 0.0578, 0.0771

distributed in the inlet bulk flow. The mass of the injected fibers in each experiment ranged from 0.4 to 1.0 mg. The airway model was placed horizontally during our experiments. The inlet of G0 was connected to the mixing chamber, while each daughter tube of G1 was attached with a 50-mm-diameter filter and a flowmeter. The filters were made of stainless steel with a pore size of 5  $\mu\text{m}$ . Four constant flow rates of 4, 8, 12, and 16 L/min were selected for study. Two separate flow meters ensured that flow rates into the two daughter tubes were the same during experiments (Table 1).

After each experiment, the airway model was detached from the system. The two halves of the model were placed on a customized one-dimensional moving platform. Micrographs of deposited fibers were taken using a stereo microscope (SZM-45, Nanjing Jiangnan Novel Optics Co., Ltd., China) with a digital single-lens reflex camera (EOS 600D, Canon Inc., Kaohsiung, China). Fibers deposited in the airway model, rear pipe, and filters were washed out using

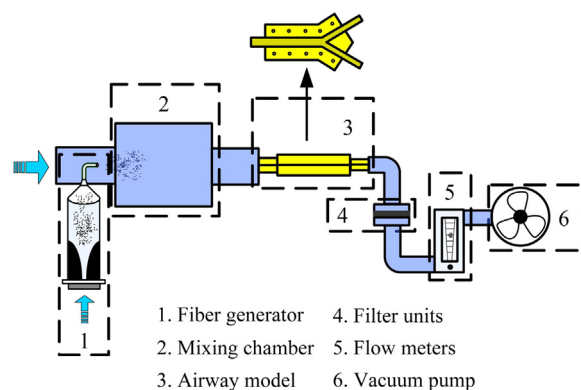


Fig. 3. Schematic diagram of the experimental setup.

an ultrasonic bath. The water solutions containing the fibers were vacuum-filtered with stainless steel filters having a diameter of 50 mm. An additional 500 mL of water was used to clean any possible residue of the sodium polyacrylate solution on the fibers during vacuum-filtering. Filters with captured fibers were weighed using an electronic analytical scale, with an accuracy of 0.01 mg (Sartorius CP225D, Data Weighing Systems Inc., Elk Grove, IL, USA), after drying in a dust-free desiccator for over 6 h. Thus, weights of fibers deposited in and penetrating through the airway bifurcation were obtained and used to calculate fiber deposition fractions under different flow rates.

#### Image-processing

Image processing is shown schematically in Fig. 4. The central parts of the micrographs were clipped out to avoid shadow and unfocused areas near their boundaries. These images were converted to gray-scale and then their gray values were reversed to facilitate analysis. Background images were calculated by the morphological opening operation using a disk-shaped structuring element based on these images. A median filter was applied to the gray value reversed images after subtracting their background images. The thresholds of gray values were then set to highlight fibers. Only simply-connected domains of these processed negative images were calculated, and a minimum bounding box algorithm was applied to these domains to obtain detailed information on fibers, i.e., pixels for fiber diameter, fiber length, and fiber orientation. A pixel threshold was set to filter out fiber debris and noise in the micrographs. Hence, fibers shorter than 14.68  $\mu\text{m}$  (aspect ratio

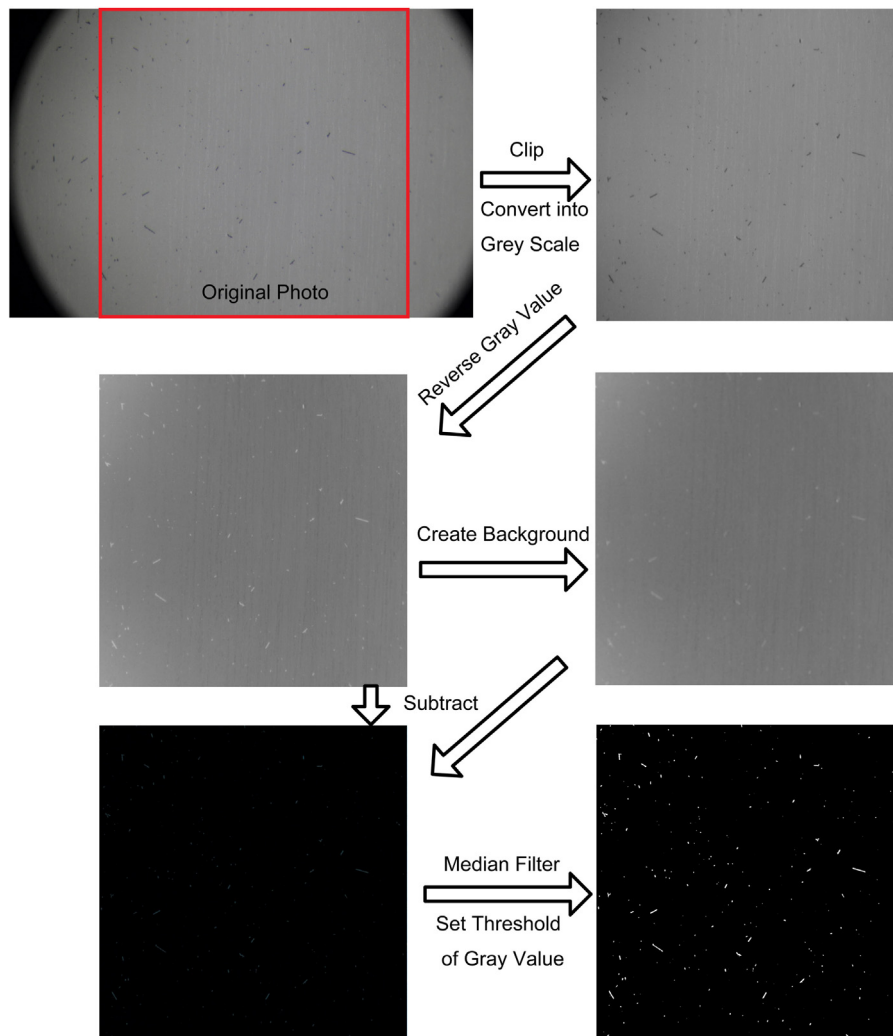


Fig. 4. Schematic diagram of image-processing method used to analyze fiber deposition and orientation information in this study.

$\beta < 2$ ) were not included in our analysis. Because long fibers have a higher probability of overlap with other fibers, it was difficult to collect enough sample information for fibers with  $\beta > 5$ . Therefore, fibers with  $\beta < 2$  or  $\beta > 5$ , comprising 18.8% and 18.2% of the total population, were excluded from this study. Finally, the pixels of fiber lengths were converted into actual lengths based on the ratio of a fiber's actual diameter to its diametric pixel. To analyze the effects of fiber length and flow rate on the distribution of the orientations of deposited fibers, the orientation angles were separated into three sets (S1–S3) based on their fiber aspect ratios: S1 for  $2 \leq \beta < 3$ ; S2 for  $3 \leq \beta < 4$ ; and S3 for  $4 \leq \beta < 5$ . Image processing and data analysis were programmed and carried out using MATLAB and VC++, respectively.

#### Particle parameters

The particle DF is defined as:

$$DF = \frac{m_{\text{deposit}}}{m_{\text{deposit}} + m_{\text{exit}}}, \quad (1)$$

where  $m_{\text{deposit}}$  is the particle mass deposited on the inner airway surfaces, and  $m_{\text{exit}}$  is the particle mass that exited the airway model. In contrast, the particle DE is a local parameter, indicating the ratio of deposited particles to all those that entered a specific region, e.g., an airway generation or bifurcation region.

The aerodynamic equivalent diameter  $d_{ae}$  of a fiber, used for determining the Stokes number, was calculated using Stöber's correlation (Stöber, 1972):

$$d_{ae} = d_{ve} \sqrt{\rho_p / (\rho_0 \kappa)}, \quad (2)$$

where  $d_{ve}$  is the volume-equivalent diameter,  $\rho_p$  is the density of fiber,  $\rho_0$  is the density of water, and  $\kappa$  is the dynamic shape factor. Assuming the fibers are orientated randomly in air,  $\kappa$  is given by:

$$\frac{1}{\kappa} = \frac{1}{3\kappa_{\parallel}} + \frac{2}{3\kappa_{\perp}}, \quad (3)$$

where  $\kappa_{\parallel}$  and  $\kappa_{\perp}$  are the dynamic shape factors for fibers orientated parallel and perpendicular to the flow, respectively (Su & Cheng, 2005). Specifically, the dynamic shape factors  $\kappa_{\parallel}$  and  $\kappa_{\perp}$  are defined as:

$$\kappa_{\parallel} = \frac{\frac{4}{3}(\beta^2 - 1)\beta^{-1/3}}{\frac{2\beta^2 - 1}{\sqrt{\beta^2 - 1}} \ln(\beta + \sqrt{\beta^2 - 1}) - \beta}, \quad (4)$$

and

$$\kappa_{\perp} = \frac{\frac{8}{3}(\beta^2 - 1)\beta^{-1/3}}{\frac{2\beta^2 - 3}{\sqrt{\beta^2 - 1}} \ln(\beta + \sqrt{\beta^2 - 1}) + \beta}. \quad (5)$$

The values for  $\kappa_{\parallel}$ ,  $\kappa_{\perp}$ , and  $d_{ae}$  of fibers used in this study having CMD of 7.34  $\mu\text{m}$  and CML of 22.97  $\mu\text{m}$ , are 1.211, 0.978, and 15.48  $\mu\text{m}$ , respectively.

The Stokes number used for graphing fiber deposition results is defined as:

$$St = \frac{\rho_p d_{ae}^2 U}{18\mu D}, \quad (6)$$

where  $U$  is the mean air velocity at the inlet,  $\mu$  is the dynamic viscosity of air, and  $D$  is the inlet tube diameter.

Typically, the DF increases with increasing Stokes number for micron-sized particles in pulmonary airways, when inertial impaction is the dominant deposition mechanism. Kleinstreuer et al. (2007) proposed a sedimentation parameter  $\gamma$ , defined as:

$$\gamma = \left( \frac{v_{\text{settling}}}{U} \right) \left( \frac{L}{D} \right) \cos \varphi, \quad (7)$$

where  $v_{\text{settling}}$  is the settling/terminal velocity of the particle,  $L$  is the length of the airway tube, and  $\varphi$  is the inclination angle measured relative to the horizontal ( $\varphi = 0$  in this study). Given that our particles are non-spherical, the terminal velocity is calculated based on the equation proposed by Haider and Levenspiel (1989):

$$v_{\text{settling}} = \frac{v_*}{\left[ \frac{\rho_f^2}{g\mu(\rho_p - \rho_f)} \right]^{1/3}}, \quad (8)$$

where  $g$  is the gravitational acceleration,  $\rho_f$  is the density of the fluid, and  $v_*$  is the dimensionless terminal velocity, defined as:

$$v_* = \left[ \frac{18}{d_*^2} + \frac{(2.3348 - 1.7439\phi)}{d_*^{0.5}} \right]^{-1} \quad 0.5 \leq \phi \leq 1, \quad (9)$$

where  $\phi$  is the particle sphericity, and  $d_*$  is the dimensionless particle diameter, given by:

$$d_* = d_{ve} \left[ \frac{g\rho_f(\rho_p - \rho_f)}{\mu^2} \right]^{1/3}. \quad (10)$$

The sedimentation parameter  $\gamma$  is more suitable than the Froude number,  $Fr = U/\sqrt{gD}$ , for determining the dominant deposition mechanism in small airways, where gravity may measurably affect particle deposition (Kleinstreuer et al., 2007). It is suggested that the inertial impaction is dominant for  $\gamma < 10^{-3}$ , gravitational sedimentation needs to be included for  $10^{-3} < \gamma < 10^{-1}$ , while sedimentation is dominant for  $\gamma > 10^{-1}$ . In this study, the sedimentation parameter has values from 0.0487 to 0.195 for flow rates from 16 to 4 L/min.

### Computational analysis

An unstructured tetrahedral mesh with multiple boundary layers and different effective diameter models for particles was constructed to compare simulation results for fibrous particles with our experimental results. A similar comparison of different effective diameter models has been carried out to evaluate non-spherical particle deposition in other studies (Feng & Kleinstreuer, 2013). Employing the same geometry and flow conditions as our experimental setup, the Navier–Stokes equations and Newton's second law of motion were solved using Fluent software (Ansys, Canonsburg, USA). Steady incompressible laminar flow was assumed. Drag and gravity were considered the main forces affecting particle motion in our simulations. Detailed descriptions of the transport equations for fluid flow and particle dynamics can be found in Kleinstreuer et al. (2007). Because the flow was assumed to be laminar and fully-developed, a parabolic velocity distribution was applied at the inlet. The particles were randomly distributed at the inlet plane. Initial velocities of these particles were set to local flow

**Table 2**  
Segmental mass balance in the daughter tubes.

Flow rate (L/min)	Fraction of the pixels of deposited fibers in each tube (%)					
	S1 ( $2 \leq \beta < 3$ )		S2 ( $3 \leq \beta < 4$ )		S3 ( $4 \leq \beta < 5$ )	
	G1a	G1b	G1a	G1b	G1a	G1b
4	50.67	49.33	48.71	51.29	43.73	56.27
8	50.90	49.10	47.47	52.53	48.10	51.90
12	52.21	47.79	54.71	45.29	52.05	47.95
16	53.79	46.21	52.20	47.80	52.01	47.99

velocity. The fluid velocity along the center line of the daughter tube near the outlet was used to test mesh independence of the simulation (Fig. 5(a)). Fig. 5(a) also shows the velocity distributions along the midplane and the cross-section predicted by a result-independent mesh. Three meshes with different element numbers were generated to examine fluid velocity along the center line. The result-independent mesh required 2.4 million elements (Fig. 5(b)). The inlet and the prism layers of the final mesh are shown in Fig. 5(c).

## Results and discussion

### Deposition experiments

As part of our verification process, the fiber mass balance in the daughter tubes was examined by counting the sum of pixels belonging to deposited fibers in the micrographs, i.e., between P12 and P16 in both daughter tubes. As shown in Table 2, it appeared that only under one condition (4 L/min; S3) was the ratio larger than 55%, but less than 60%.

Fig. 6(a) and (b) depicts the variation in DFs for different inhalation flow rates as a function of their Stokes number and sedimentation parameter, respectively. Because sedimentation was the dominant deposition mechanism at low flow rates, the DF-values decreased with increasing flow rates (Fig. 6(a)). The DF increased almost linearly with increases in the sedimentation parameter (Fig. 6(b)), consistent with deposition governed by gravitational sedimentation. In this case, the sedimentation parameter is a more suitable parameter than the Stokes number for describing fibrous particle deposition.

Sedimentation declined as the flow rate increased, and more fibers remained entrained in the airflow. Higher flow velocity may contribute to deposition by inertial impaction, although the overall DF dropped. DFs also increased with increasing Stokes number at higher flow rates, when inertial impaction became the dominant deposition mechanism. This infers there is a minimum DF for a certain Stokes number in the airway. Hofmann et al. (1995) also described such changes in deposition mechanism for a horizontally placed G15–G16 airway, using a Monte Carlo simulation. In their study, deposition of 10- $\mu\text{m}$  particles occurred on the bottom of the airways at flow rates of 10 L/min; while it shifted to the bifurcation region, when flow rate increased to 60 L/min. Balásházy, Martonen, and Hofmann (1990) reported decreases/increases in DE-curves for spherical particles, with increasing Stokes number around a bend, based on a theoretical model. As particles decrease from micron to submicron size, the DE also decreases, because of reduced particle inertia. However, as particle size continues to decrease, the role of Brownian motion in the deposition mechanism gradually increases. Thus, the DE of a 5-nm-particle is higher than for a 150-nm-particle under the same conditions (Shi, Kleinstreuer, Zhang, & Kim, 2004).

Our experimental results have implications for targeted drug delivery of non-spherical particles. Using our model, it may be possible to achieve a low DE-value in a specific airway generation by controlling the inlet conditions, and changing physical

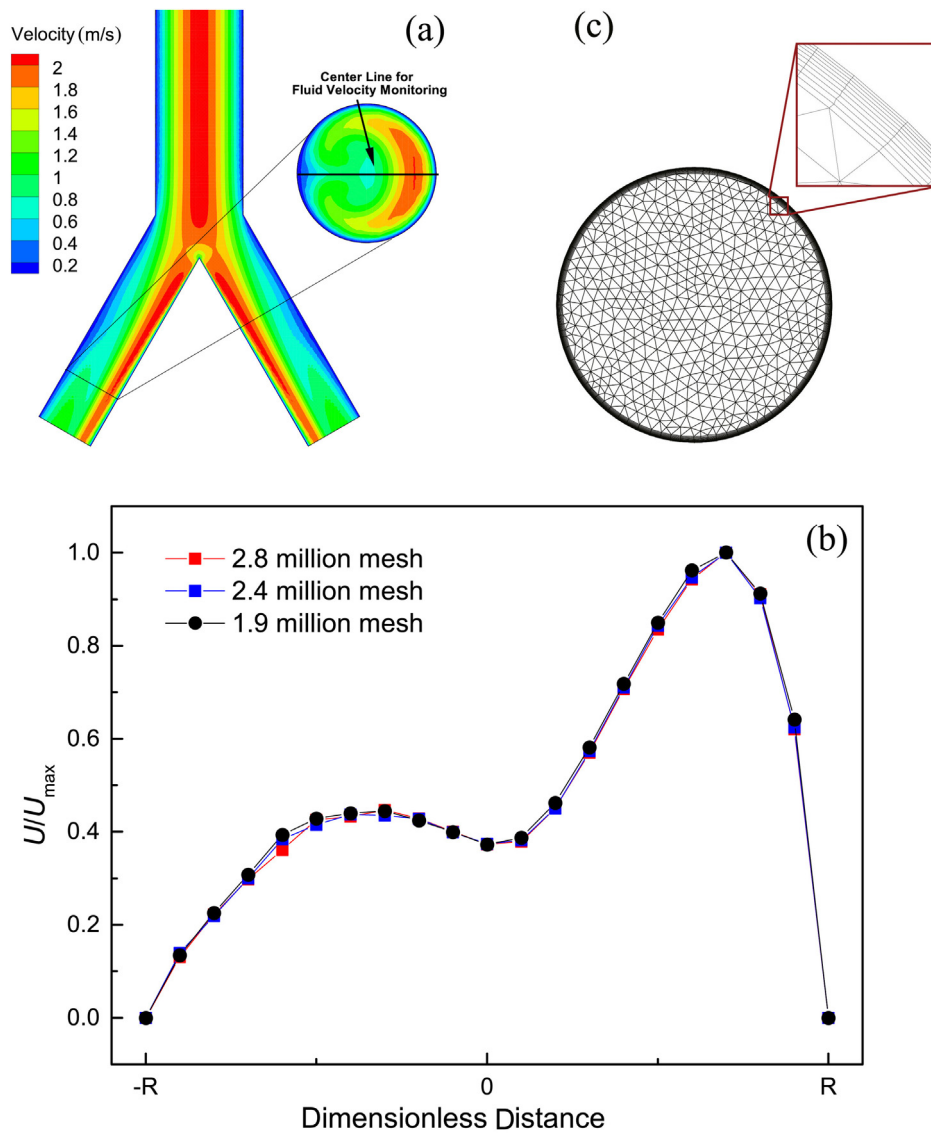


**Fig. 5.** Mesh independence test results: (a) velocity distributions and locations selected for mesh independence testing, (b) dimensionless fluid velocities for different meshes, (c) mesh constructs for the inlet and prism layers.

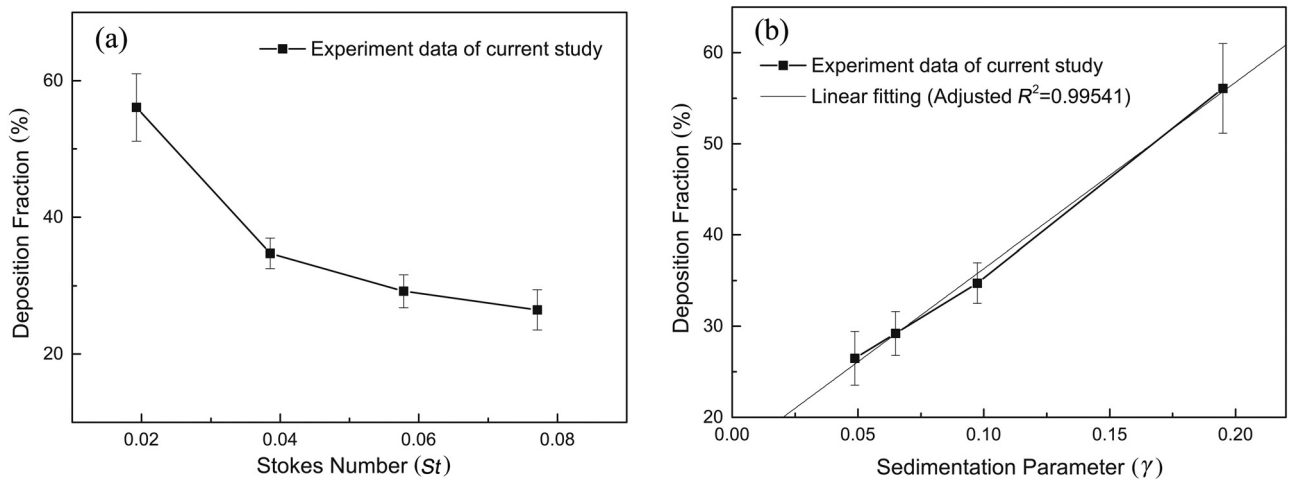


**Fig. 6.** Fiber deposition fractions under steady inhalation conditions: (a) deposition fraction vs. Stokes number and (b) deposition fraction vs. sedimentation parameter.

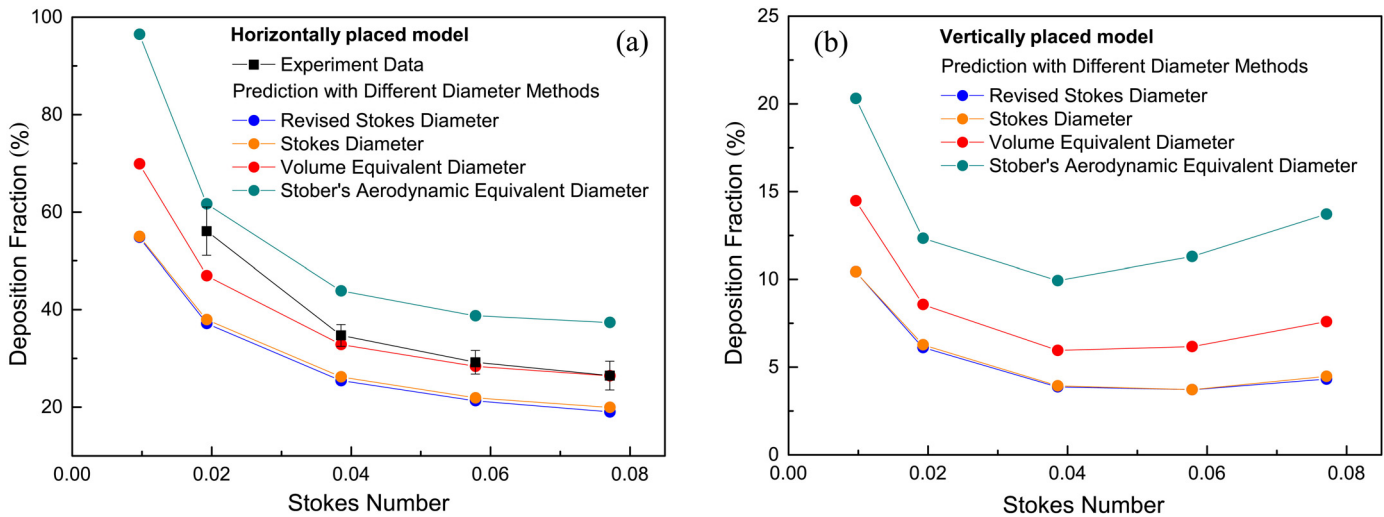


Fig. 7. Predicted deposition fractions using different sphere-equivalent diameter methods and using: (a) horizontally and (b) vertically placed airway model.

characteristics of the fibers to reduce sedimentation. In addition, regional deposition in the lower airway could be enhanced by applying an external force, e.g., a magnetic force (Martin & Finlay, 2008a, 2008b) or acoustic force (Dong, Lipkens, & Cameron, 2006; Fan, Yang, & Kim, 2013; Hoffmann & Koopmann, 1996). A numerical investigation (Feng & Kleinstreuer, 2013) showed that the stability of fibrous particle is related to the local velocity gradient. Thus, disturbances linked to an external force, e.g., a longitudinal wave caused by an acoustic force, may increase local deposition of fibrous particles.

#### Numerical simulations

Several sphere-equivalent diameter models were considered in our numerical study to track the fiber motion and deposition. Specifically, the volume-equivalent diameter, the Stokes equivalent diameter (Shapiro & Goldenberg, 1993), a revised Stokes equivalent diameter (Feng & Kleinstreuer, 2013), and Stöber's aerodynamic diameter (Stöber, 1972) were used for simulations with the airway model placed horizontally (Fig. 7(a)), as well as vertically (Fig. 7(b)). Surprisingly, the volume-equivalent diameter appeared to be the best approximation for fiber deposition linked to sedimentation and impaction (Fig. 7(a)). The prediction for a vertical bifurcation in Fig. 7(b) showed decreases/increases for DF, similar to those described above. A series of simulations were carried out with the bifurcation consisting of four sections: a parent tube, a junction, and the two daughter tubes. For a flow rate of 12 L/min, with Stöber's aerodynamic diameter as the sphere-equivalent diameter, local DEs under horizontal vs. vertical configurations were explored. Results are summarized in Table 3. Clearly, the gravitational effect (especially in G0) becomes dominant, when the airways are horizontal,

indicating the importance role that a subject's body position plays in deposition of particles in airways.

#### Matching of Stokes number and sedimentation parameters

For any given Stokes number and sedimentation parameter, which define fiber diameter and length, the inlet flow rate can be calculated from Eq. (6) or based on variables from Eqs. (7) to (10) for different airway generations. If the nasal/oral flow rate is within a reasonable range, i.e., 15–120 L/min, then similar deposition characteristics occur within that generation for matched Stokes number and sedimentation parameter, as demonstrated in our experiments. Table 4 provides an example for a Stokes number of 0.0193 (i.e., 4 L/min condition in our experiments) for fibrous carbon particles with  $\rho_p = 1780 \text{ kg/m}^3$ ,  $d_p = 2.5 \text{ }\mu\text{m}$ ,  $l_p = 10 \text{ }\mu\text{m}$ . Similarly, airway generations within reasonable flow rates can be found by matching the sedimentation parameter. The results by matching Stokes numbers and sedimentation parameters are summarized in Table 5 for fibrous carbon particles, with  $d_p = 2.5 \text{ }\mu\text{m}$  and  $l_p = 10 \text{ }\mu\text{m}$ .

Clearly, sedimentation contributes significantly to particle deposition. Thus, our experimental DEs could be used to estimate the deposition characteristics of fibrous particles in the lower airways, e.g., G6–G15, by only considering the sedimentation parameter. Even though inertial impaction (Stokes number) needs to be taken into account, this study's results could be successfully used for G8–G11. Note that the inclination angles  $\varphi$  used in Tables 4 and 5 were  $0^\circ$ . Therefore, the results of this study could be applied to a wider range of airway generation for the same sedimentation parameters (see Eq. (7)), if the inclination angles of the matched condition are not  $0^\circ$ .

#### Fiber orientations

Micrographs showed that the number of deposited fibers at each observation point on the upside airway was very limited, usually less than five fibers. Therefore, our analysis of fiber orientation was based only on micrographs of the downside airway. This also supports our conclusion that gravitational sedimentation is the predominant deposition process in our experiments. The absolute values of the orientation angles (i.e.,  $|\theta|$ ) for each experiment were divided into three groups to produce orientation distributions, using  $30^\circ$  intervals (i.e.,  $0^\circ$ – $30^\circ$ ,  $30^\circ$ – $60^\circ$ ,  $60^\circ$ – $90^\circ$ ). The mean

Table 3

Predicted local deposition efficiencies under vertical and horizontal conditions. (The deposition fractions of deposited fibers were 11.26% and 38.81 in vertical and horizontal configurations, respectively.)

Location	DE (%)	
	Vertical	Horizontal
Bifurcation	5.11	3.62
G0	0.17	27.02
G1a	2.88	4.03
G1b	3.10	4.13

**Table 4**  
Matching Stokes number ( $St = 0.0193$ ) for carbon fibers ( $\rho_p = 1780 \text{ kg/m}^3$ ,  $d_p = 2.5 \text{ }\mu\text{m}$ ,  $l_p = 10 \text{ }\mu\text{m}$ ).

Airway generation	Diameter (mm)	Area ( $\text{m}^2$ )	Local flow rate ( $\text{m}^3/\text{s}$ )	Nasal/oral flow rate (L/min)
0	18	$2.54 \times 10^{-4}$	$5.14 \times 10^{-4}$	30.86
1	12.2	$1.17 \times 10^{-4}$	$1.60 \times 10^{-4}$	19.22
2	8.3	$5.41 \times 10^{-5}$	$5.04 \times 10^{-5}$	12.10
3	5.6	$2.46 \times 10^{-5}$	$1.55 \times 10^{-5}$	7.43
4	4.5	$1.59 \times 10^{-5}$	$8.04 \times 10^{-6}$	7.72
5	3.5	$9.62 \times 10^{-6}$	$3.78 \times 10^{-6}$	7.26
6	2.8	$6.16 \times 10^{-6}$	$1.94 \times 10^{-6}$	7.43
7	2.3	$4.15 \times 10^{-6}$	$1.07 \times 10^{-6}$	8.24
8	1.86	$2.72 \times 10^{-6}$	$5.68 \times 10^{-7}$	8.72
9	1.54	$1.86 \times 10^{-6}$	$3.22 \times 10^{-7}$	9.90
10	1.3	$1.33 \times 10^{-6}$	$1.94 \times 10^{-7}$	11.91
11	1.09	$9.33 \times 10^{-7}$	$1.14 \times 10^{-7}$	14.03
12	0.95	$7.09 \times 10^{-7}$	$7.56 \times 10^{-8}$	18.58
13	0.82	$5.28 \times 10^{-7}$	$4.86 \times 10^{-8}$	23.90
14	0.74	$4.30 \times 10^{-7}$	$3.57 \times 10^{-8}$	35.13
15	0.66	$3.42 \times 10^{-7}$	$2.54 \times 10^{-8}$	49.85
16	0.6	$2.83 \times 10^{-7}$	$1.91 \times 10^{-8}$	74.91
17	0.54	$2.29 \times 10^{-7}$	$1.39 \times 10^{-8}$	109.22
18	0.5	$1.96 \times 10^{-7}$	$1.10 \times 10^{-8}$	173.40
19	0.47	$1.73 \times 10^{-7}$	$9.16 \times 10^{-9}$	288.05
20	0.45	$1.59 \times 10^{-7}$	$8.04 \times 10^{-9}$	505.64
21	0.43	$1.45 \times 10^{-7}$	$7.01 \times 10^{-9}$	882.34
22	0.41	$1.32 \times 10^{-7}$	$6.08 \times 10^{-9}$	1529.72
23	0.41	$1.32 \times 10^{-7}$	$6.08 \times 10^{-9}$	3059.43

**Table 5**  
Reasonable flow rates (L/min) within each airway generation in Weibel's airway model, calculated by matching Stokes number ( $St$ ) or sedimentation parameter ( $\gamma$ ) and at different inlet flow rates (L/min).

Airway generation	Calculated reasonable flow rate within each airway generation							
	4		8		12		16	
	$St=0.0193$	$\gamma=0.01951$	$St=0.0385$	$\gamma=0.00975$	$St=0.0578$	$\gamma=0.00650$	$St=0.0771$	$\gamma=0.00488$
G0	30.9	-	61.7	-	92.6	16.6	-	22.2
G1	19.2	-	38.4	-	57.7	-	76.9	-
G2	-	-	24.2	-	36.3	-	48.4	-
G3	-	-	-	-	22.3	-	29.7	-
G4	-	-	15.4	-	23.1	-	30.9	-
G5	-	-	-	-	21.8	-	29.0	-
G6	-	-	-	-	22.3	-	29.7	16.5
G7	-	-	16.5	-	24.7	17.2	33.0	23.0
G8	-	-	17.4	15.6	26.2	23.4	34.9	31.3
G9	-	-	19.8	21.8	29.7	32.8	39.6	43.7
G10	-	15.7	23.8	31.4	35.7	47.1	47.6	62.8
G11	-	22.3	28.1	44.7	42.1	67.0	56.1	89.3
G12	18.6	32.9	37.2	65.9	55.8	98.8	74.3	-
G13	23.9	46.5	47.8	90.3	71.7	-	95.6	-
G14	35.1	71.5	70.3	-	105.4	-	-	-
G15	49.9	110.9	99.7	-	-	-	-	-
G16	74.9	-	-	-	-	-	-	-
G17	109.2	-	-	-	-	-	-	-

**Table 6**  
Sedimentation parameters occurring under different flow rate conditions and fiber lengths.

Fiber length	Flow rate (L/min)			
	4	8	12	16
Average value of all fibers	0.195	0.0974	0.0649	0.0487
S1 ( $2 \leq \beta < 3$ )				
In G0	0.168	0.0841	0.0560	0.0420
In G1	0.0912	0.0456	0.0304	0.0228
S2 ( $3 \leq \beta < 4$ )				
In G0	0.209	0.104	0.0698	0.0524
In G1	0.114	0.0568	0.0379	0.0284
S3 ( $4 \leq \beta < 5$ )				
In G0	0.247	0.123	0.0822	0.0617
In G1	0.134	0.0770	0.0446	0.0335

fiber length was used to calculate the sedimentation parameter for each data group (Table 6).

*Average absolute orientation angle  $|\bar{\theta}|$  of deposited fibers*

Fig. 8 depicts the average absolute orientation angle of the deposited fibers in the bifurcating airway model under different conditions. Each condition has three data points, representing the three fiber lengths, S1–S3.

All data points for the two generations were closely located within a linear region, except for data having the 4 L/min condition in G0. Linear regression was applied to these data to evaluate differences in  $|\bar{\theta}|$  between G0 and G1. Two fitted curves were regressed. These two curves share a similar slope, but have different intercept values. The intercept difference between #1 and #2 indicates that parallelism of the fibers was diminished in the daughter tubes. The enclave of data for the 4-L/min condition in G0 may reflect an

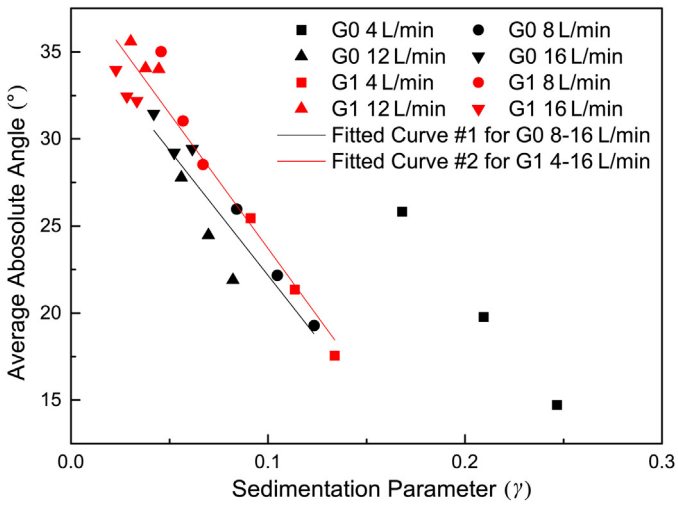


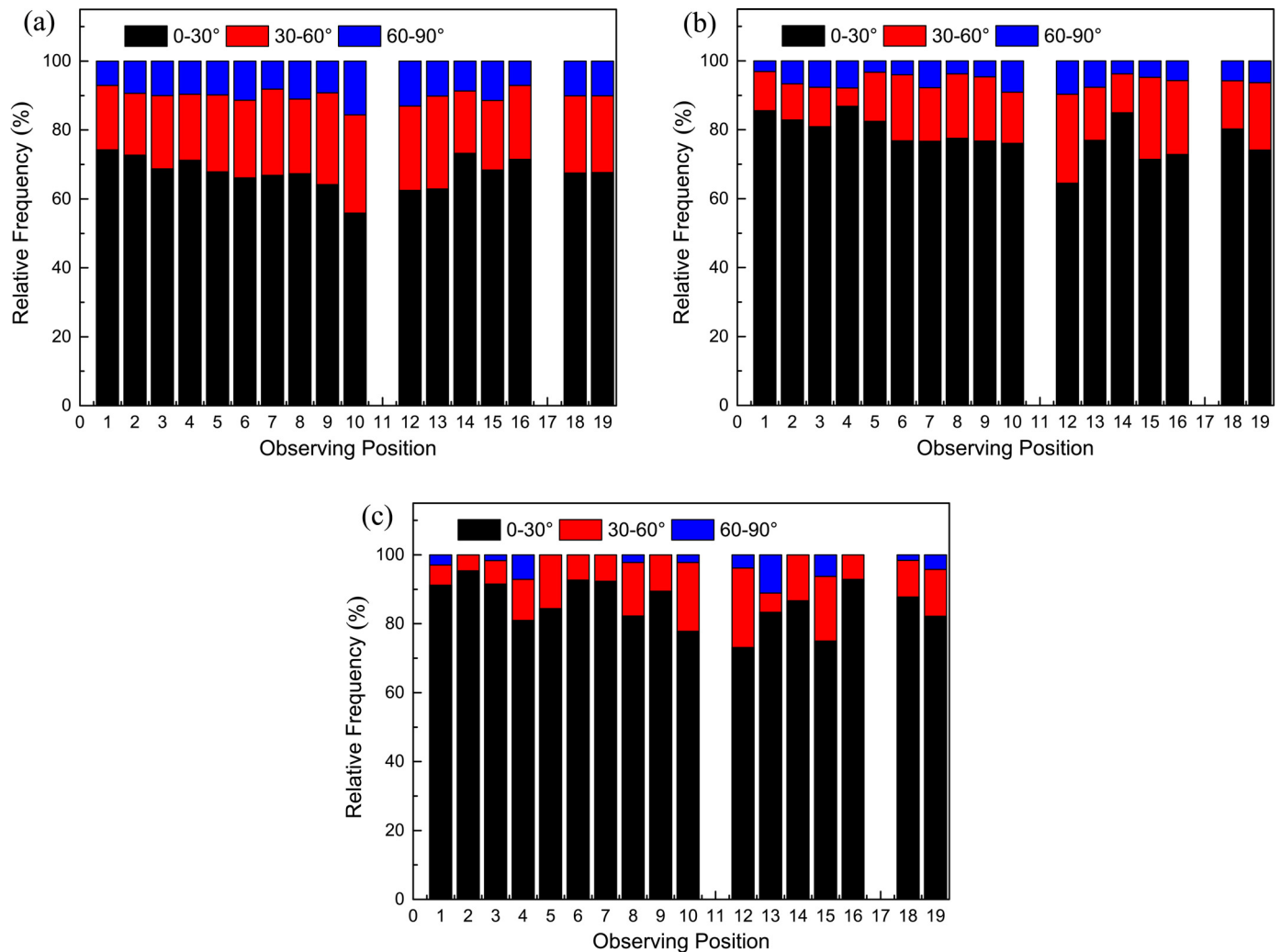
**Fig. 8.** Average absolute orientation angle  $|\bar{\theta}|$  in a sequentially bifurcating airway model. Fitted curves are in the form of  $|\bar{\theta}| = a\gamma + b$ . Constants are  $a = -143.75$ ,  $b = 36.54$  for Curve #1 ((root mean square error of  $|\bar{\theta}| = 1.674$ );  $a = -155.13$ ,  $b = 39.22$  for Curve #2 (root mean square error of  $|\bar{\theta}| = 1.482$ ).

increase in gravitational effects. This suggests that sedimentation dominates in regions with  $\gamma > 0.15$  for this type of carbon fiber. It is also worth noting that the change in  $|\bar{\theta}|$  caused by fiber length, linearly relates to variation in  $\gamma$ , when comparing across the three fiber length data sets under equivalent generations and flow rates.

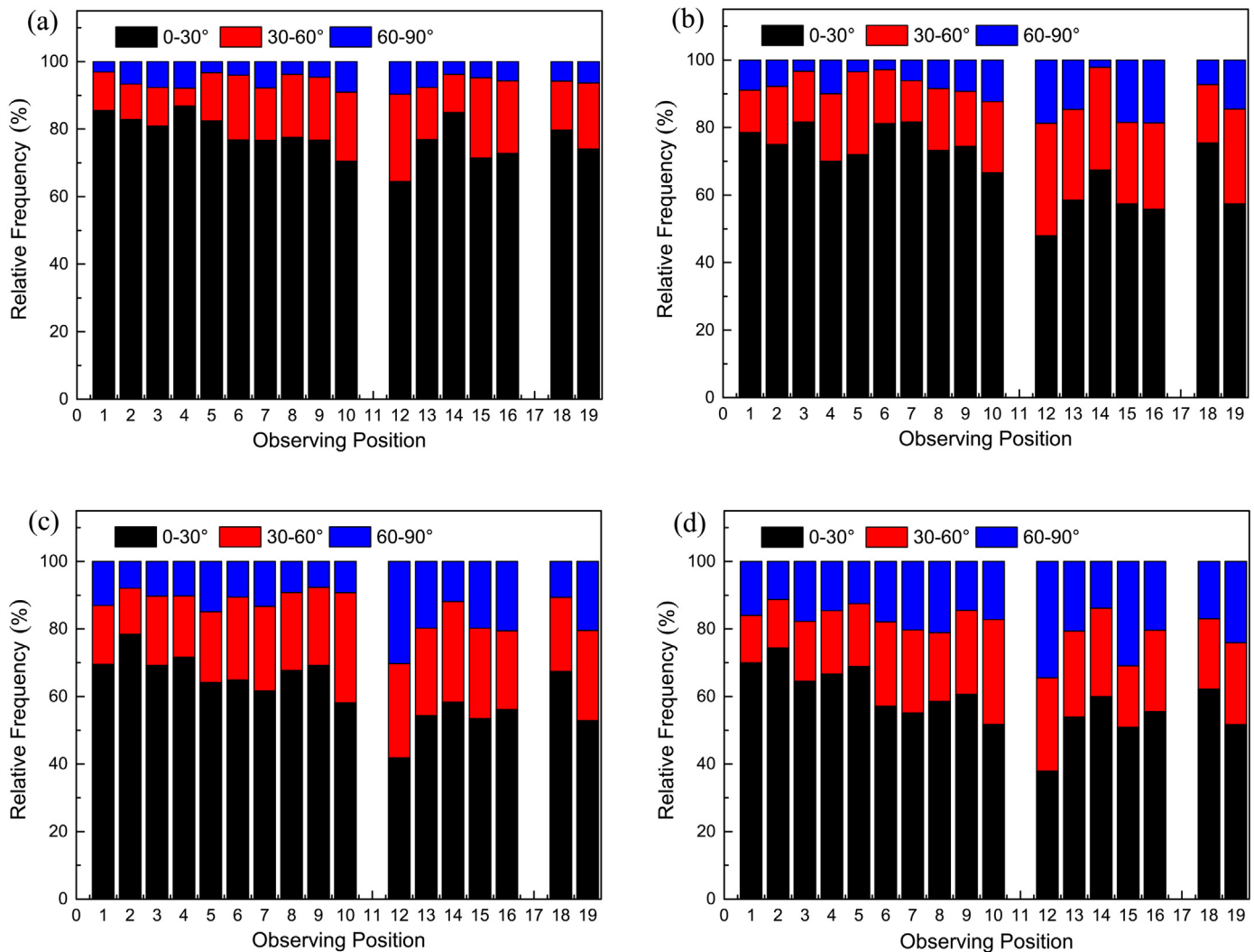
*Fiber length effect*

Fig. 9 compares the fiber orientation distributions of different fiber length data sets for a flow rate of 4 L/min. P18 and P19 are average values of all three angular orientation groups within G0 and G1, respectively. Although airflow was laminar ( $Re = 315$ ), the deposited fibers were not exactly parallel to flow direction. However, most orientation angles (i.e., for >60% of particles) were within the range between  $0^\circ$  and  $30^\circ$ . This is in accord with direct measurements of the orientation distributions of fibers in laminar shear flow (Bernstein & Shapiro, 1994). Discrepancies in direct measurements may be caused by the bifurcating flow structure, as well as fiber rotation during deposition along airway surfaces.

The parallelism of the deposited fibers in G0 rose with increasing fiber length (Fig. 9). The average relative frequency of  $\theta$  between  $0^\circ$  and  $30^\circ$  in G0 (i.e., P18) was 67.7% (Fig. 9(a)), while it increased to 74.1% (Fig. 9(b)), and finally to 82.2% (Fig. 9(c)), as fiber length increased. Likewise, parallelism also improved in G1, as fiber length increased. Feng and Kleinstreuer's (2013) numerical investigation



**Fig. 9.** Orientation distributions of deposited fibers with different lengths S1–S3 under 4 L/min: (a) S1 ( $2 \leq \beta < 3$ ), (b) S2 ( $3 \leq \beta < 4$ ), and (c) S3 ( $4 \leq \beta < 5$ ). P18 and P19 are average values of all three angular orientation groups within G0 and G1, respectively.



**Fig. 10.** Orientation distributions of deposited S2 ( $3 \leq \beta < 4$ ) fibers under different flow rates: (a) 4 L/min, (b) 8 L/min, (c) 12 L/min, and (d) 16 L/min. P18 and P19 are average values of all three angular orientation groups within G0 and G1, respectively.

showed that longer fibers, or fibers with lower sphericity, aligned better with the flow. However, the average orientation distributions within G0 and G1 were different under different fiber length conditions. The average orientation angle for deposited fibers with  $0^\circ$ – $30^\circ$  group for longer fibers decreased approximately  $5^\circ$  because of the bifurcation (Fig. 9(b) and (c)). In contrast, the average relative frequencies of the three different orientation groups were almost the same for P18 and P19 (Fig. 9(a)). Most likely, short fibers align themselves more rapidly with the axial flow, even under the impact of secondary flow near the bifurcation region; while long fibers have lower rotational speed, with larger inertia, leading to greater variation in their orientations.

From groups S1 to S3, the average relative frequency of the  $0^\circ$ – $30^\circ$  orientation group increased by 20.3% in the parent tube (G0), but decreased by 11.8% and 8.5% for the  $30^\circ$ – $60^\circ$  and  $60^\circ$ – $90^\circ$  groups in G0, respectively. Similarly, the  $30^\circ$ – $60^\circ$  orientation group experienced more of decrease in average relative frequency than the  $60^\circ$ – $90^\circ$  group in G1, with decreases of 8.7% and 5.8%, respectively.

Because the airflow splits into two branches at the bifurcation point, more fibers deviated from the axial direction as they approached the bifurcation. Therefore, the relative frequency of the  $0^\circ$ – $30^\circ$  group decreased along the G0 tube from P1 to P10; thus, P10 had the lowest relative frequency of this orientation group in G0 for

all fiber lengths. In the parent tube, the relative frequencies of the  $60^\circ$ – $90^\circ$  group remained comparatively steady, except at P10, with values of  $9.5 \pm 2.4\%$ ,  $5.4 \pm 2.3\%$ , and  $1.6 \pm 1.5\%$  for the S1, S2, and S3 datasets, respectively. P10 was the only location where the relative frequency of the  $60^\circ$ – $90^\circ$  group showed a distinct increase. Thus, variation in fiber angles mainly occurred within  $60^\circ$  of the tube.

Separation of the airflow after the bifurcation skewed velocity profiles, i.e., as it entered the G1 tubes. Details of such skewed velocity profiles in lung models are well documented (Chen, Zhong, Sun, Jin, & Zhou, 2012; Yang, Liu, & Luo, 2006; Zhang, Kleinstreuer, & Kim, 2001; Zhang, Kleinstreuer, & Kim, 2002). This indicates that comparatively strong secondary flow occurs along the interior side of the airway toward the lateral side. As a result of this secondary flow, the relative frequencies of the  $0^\circ$ – $30^\circ$  group at P12 were the lowest within G1. Because the decentralized flow becomes less pronounced as it moves deeper into G1, the frequencies of  $0^\circ$ – $30^\circ$  group gradually increased from P12 to P16, as shown in Fig. 9(a)–(c). Similar to the parent tube, changes in the relative frequencies of the  $60^\circ$ – $90^\circ$  group were not pronounced.

#### Flow rate effect

Fig. 10 shows the effect of flow rate on the orientation of deposited S2 ( $3 \leq \beta < 4$ ) fibers. Generally, parallelism of the deposited fibers decreased under elevated flow rates. The average

relative frequencies of the  $0^\circ$ – $30^\circ$  group in G0 and G1 at 4 L/min were 79.7% and 74.1%, respectively (Fig. 10(a)). These frequencies dropped to 75.4% and 57.4% at 8 L/min, declining to 67.4% and 52.8% at 12 L/min condition, and finally to 62.1% and 51.6% at 16 L/min (Fig. 10(b)–(d)). The average relative frequencies of the  $30^\circ$ – $60^\circ$  group increased by 6.3% and 4.7% in G0 and G1, while the values of the  $60^\circ$ – $90^\circ$  group increased by 11.2% and 17.7%, respectively, as flow rate increased from 4 to 16 L/min. Thus, the increase in flow rate had a higher impact on larger orientation angles, contrasting with the effect of fiber length.

The changes in relative frequency of fiber orientation along the length of the airways under different flow rates were similar to descriptions in the previous section on fiber length. Parallelism slowly decreased as fibers traveled with the airflow toward the bifurcation. After the bifurcation, parallelism changed abruptly, but recovered gradually.

## Conclusions

Fibrous particle deposition experiments in an idealized single-bifurcation airway model were carried out for a range of sedimentation parameters, covering  $0.0228 < \gamma < 0.247$ . The depositional process was mainly controlled by gravitational sedimentation. The DFs of fibrous particles were measured and the orientations of deposited fiber were quantitatively determined using an image-processing method. Fiber DFs, DEs and orientation information provide new data useful for the validation of numerical models. Our computer simulations, employing several sphere-equivalent diameter models for the fibers, provided a link between our experimental results and Stokes number. Using the volume-equivalent diameter model, the experimental fiber-deposition data generated in this study for the horizontal bifurcation configuration were replicated. Additionally, new simulations explored particle deposition in an airway with a vertically placed bifurcation. Based on results from both our experimental and computational study, we conclude:

- (1) Gravitational sedimentation cannot be neglected under conditions with  $0.0228 < \gamma < 0.247$ . The DF of fibrous particles in the horizontally placed airway decreases with an increase in  $St$ . Therefore, DFs of fibrous particle should have a minimum DE-value in the lower airway bifurcations.
- (2) DFs increase almost linearly as  $\gamma$  increases. Thus,  $\gamma$  appears to be more suitable than  $St$  for describing changes in DF of fibrous particles in the range  $0.0228 < \gamma < 0.247$ .
- (3) Computational analyses show that gravitational effects are dominant in bifurcations with horizontal configurations, implying that a subject's body position affects depositional processes in airways.
- (4) Matching results for certain values of  $St$  and  $\gamma$  suggests that the deposition characteristics in our experiments also could be used to estimate fiber deposition in the lower airways, e.g., in the G8–G11 region for fibers with  $d_p = 2.5 \mu\text{m}$  and  $l_p = 10 \mu\text{m}$ .
- (5) The average absolute orientation angle  $|\bar{\theta}|$  of deposited fibers linearly decreased with increasing  $\gamma$  over the range  $0.0228 < \gamma < 0.15$ . However, the  $|\bar{\theta}|$ -value does not have a linear relationship, when  $\gamma$  is larger than 0.15.
- (6) The orientations of most deposited fibers were quasi-parallel to the mainstream airflow. However, there were orientations of deposited fibers that deviated from the axial direction. The fraction of these rotated fibers is affected by fiber length, flow rate, and their location within the airway. Specifically:
  - a) longer fibers maintained better parallelism to the axial flow;
  - b) higher airflow rates decreased parallelism of fibers; and

- c) bifurcations in the airway decreased the parallelism of fibers, i.e., parallelism changed markedly as fibers moved toward the bifurcation, but recovered as they traveled into the daughter tube after the bifurcation point.

## Acknowledgements

We acknowledge the financial support of the Foundation for the National Natural Science Foundation of China (No. 51176035), and Author of National Excellent Doctoral Dissertation of China (No. 201040). In addition, financial support was provided to Xiaole Chen under the Research and Innovation Project for College Graduates of Jiangsu Province (CXZZ12.0099), the Fundamental Research Funds for the Central Universities, China Scholarship Council (No. 201306090085), and Scientific Research Foundation of Graduate School of Southeast University (No. YBJJ1209). The experience gained by Xiaole Chen as a CSC-supported Visiting Student in the Computational Multi-Physics Lab (MAE Dept., NC State University, Raleigh, USA) is also acknowledged. Table 3, Figs. 5 and 7 were provided by Josin Tom, based on his spring 2015 course-project report for MAE558. Professor Goodarz Ahmadi at Clarkson University (Clarkson, USA) provided advice for our experimental set-up, and Professor Yong Lu at Southeast University provided guidance in programming the image-processing method.

## References

- Balaszazy, I., Martonen, T. B., & Hofmann, W. (1990). Inertial impaction and gravitational deposition of aerosols in curved tubes and airway bifurcations. *Aerosol Science and Technology*, 13, 308–321.
- Bernstein, O., & Shapiro, M. (1994). Direct determination of the orientation distribution function of cylindrical particles immersed in laminar and turbulent shear flows. *Journal of Aerosol Science*, 25, 113–136.
- Blake, T., Castranova, V., Schwegler-Berry, D., Baron, P., Deye, G. J., Li, C., et al. (1998). Effect of fiber length on glass microfiber cytotoxicity. *Journal of Toxicology and Environmental Health*, 54(Part A), 243–259.
- Cavallo, D., Campopiano, A., Cardinali, G., Casciardi, S., De Simone, P., Kovacs, D., et al. (2004). Cytotoxic and oxidative effects induced by man-made vitreous fibers (MMVFs) in a human mesothelial cell line. *Toxicology*, 201, 219–229.
- Champion, J. A., & Mitragotri, S. (2006). Role of target geometry in phagocytosis. *Proceedings of the National Academy of Sciences of the United States of America*, 103, 4930–4934.
- Chen, X., Zhong, W., Sun, B., Jin, B., & Zhou, X. (2012). Study on gas/solid flow in an obstructed pulmonary airway with transient flow based on CFD–DPM approach. *Powder Technology*, 217, 252–260.
- Dong, S., Lipkens, B., & Cameron, T. (2006). The effects of orthokinetic collision, acoustic wake, and gravity on acoustic agglomeration of polydisperse aerosols. *Journal of Aerosol Science*, 37, 540–553.
- Fan, F., Yang, X., & Kim, C. N. (2013). Direct simulation of inhalable particle motion and collision in a standing wave field. *Journal of Mechanical Science and Technology*, 27, 1707–1712.
- Feng, Y., & Kleinstreuer, C. (2013). Analysis of non-spherical particle transport in complex internal shear flows. *Physics of Fluids*, 25, 091904.
- Haider, A., & Levenspiel, O. (1989). Drag coefficient and terminal velocity of spherical and nonspherical particles. *Powder Technology*, 58, 63–70.
- Herzhaft, B., & Guazzelli, . (1999). Experimental study of the sedimentation of dilute and semi-dilute suspensions of fibres. *Journal of Fluid Mechanics*, 384, 133–158.
- Hodgson, J. T., & Darnton, A. (2000). The quantitative risks of mesothelioma and lung cancer in relation to asbestos exposure. *Annals of Occupational Hygiene*, 44, 565–601.
- Hofmann, W., Balaszazy, I., & Koblinger, L. (1995). The effect of gravity on particle deposition patterns in bronchial airway bifurcations. *Journal of Aerosol Science*, 26, 1161–1168.
- Hoffmann, T. L., & Koopmann, G. H. (1996). Visualization of acoustic particle interaction and agglomeration: Theory and experiments. *The Journal of the Acoustical Society of America*, 99, 2130–2141.
- Inthavong, K., Wen, J., Tian, Z., & Tu, J. (2008). Numerical study of fibre deposition in a human nasal cavity. *Journal of Aerosol Science*, 39, 253–265.
- Kelly, J. T., Asgharian, B., Kimbell, J. S., & Wong, B. A. (2004). Particle deposition in human nasal airway replicas manufactured by different methods. Part I: Inertial regime particles. *Aerosol Science and Technology*, 38, 1063–1071.
- Kleinstreuer, C., & Feng, Y. (2013). Computational analysis of non-spherical particle transport and deposition in shear flow with application to lung aerosol dynamics—A review. *Journal of Biomechanical Engineering*, 135, 021008.
- Kleinstreuer, C., Zhang, Z., & Kim, C. S. (2007). Combined inertial and gravitational deposition of microparticles in small model airways of a human respiratory system. *Journal of Aerosol Science*, 38, 1047–1061.

- Kulkarni, P., Baron, P. A., & Willeke, K. (2011). *Aerosol measurement: Principles, techniques and applications*. New York: John Wiley & Sons.
- LeMasters, G. K., Lockey, J. E., Yiin, J. H., Hilbert, T. J., Levin, L. S., & Rice, C. H. (2003). Mortality of workers occupationally exposed to refractory ceramic fibers. *Journal of Occupational and Environmental Medicine*, 45, 440–450.
- Marijnissen, J., Zeckendorf, A., Lemkowitz, S., & Bibo, H. (1991). Transport and deposition of uniform respirable fibres in a physical lung model. *Journal of Aerosol Science*, 22, S859–S862.
- Marsh, G. M., Gula, M. J., Youk, A. O., Buchanich, J. M., Churg, A., & Colby, T. V. (2001). Historical cohort study of US man-made vitreous fiber production workers: II. Mortality from mesothelioma. *Journal of Occupational and Environmental Medicine*, 43, 757–766.
- Martin, A. R., & Finlay, W. H. (2008a). Alignment of magnetite-loaded high aspect ratio aerosol drug particles with magnetic fields. *Aerosol Science and Technology*, 42, 295–298.
- Martin, A. R., & Finlay, W. H. (2008b). Enhanced deposition of high aspect ratio aerosols in small airway bifurcations using magnetic field alignment. *Journal of Aerosol Science*, 39, 679–690.
- Mossman, B. T., & Churg, A. (1998). Mechanisms in the pathogenesis of asbestosis and silicosis. *American Journal of Respiratory and Critical Care Medicine*, 157, 1666–1680.
- Myojo, T. (1987). Deposition of fibrous aerosol in model bifurcating tubes. *Journal of Aerosol Science*, 18, 337–347.
- Myojo, T. (1990). The effect of length and diameter on the deposition of fibrous aerosol in a model lung bifurcation. *Journal of Aerosol Science*, 21, 651–659.
- Myojo, T., & Takaya, M. (2001). Estimation of fibrous aerosol deposition in upper bronchi based on experimental data with model bifurcation. *Industrial Health*, 39, 141–149.
- Sakai, H., Watanabe, Y., Sera, T., Yokota, H., & Tanaka, G. (2015). Visualization of particle deposition in human nasal cavities. *Journal of Visualization*, 18(2), 349–357.
- Shanley, K. T., Ahmadi, G., Hopke, P. K., & Cheng, Y. S. (2009). Fibrous and spherical particle transport and deposition in the human nasal airway: A computational fluid dynamics model. In *ASME 2009 Fluids Engineering Division Summer Meeting* (pp. 2139–2148). American Society of Mechanical Engineers.
- Shapiro, M., & Goldenberg, M. (1993). Deposition of glass fiber particles from turbulent air flow in a pipe. *Journal of Aerosol Science*, 24, 65–87.
- Shi, H., Kleinstreuer, C., Zhang, Z., & Kim, C. (2004). Nanoparticle transport and deposition in bifurcating tubes with different inlet conditions. *Physics of Fluids (1994–present)*, 16, 2199–2213.
- Simone, E. A., Dziubla, T. D., & Muzykantov, V. R. (2008). Polymeric carriers: Role of geometry in drug delivery. *Expert Opinion on Drug Delivery*, 5, 1283–1300.
- Stöber, W. (1972). Dynamic shape factors of nonspherical aerosol particles. In T. T. Mercer, P. E. Morrow, & W. Stöber (Eds.), *Assessment of airborne particles* (pp. 249–289). Springfield, IL: Charles C. Thomas.
- Su, W. C., & Cheng, Y. S. (2005). Deposition of fiber in the human nasal airway. *Aerosol Science and Technology*, 39, 888–901.
- Su, W. C., & Cheng, Y. S. (2006). Deposition of fiber in a human airway replica. *Journal of Aerosol Science*, 37, 1429–1441.
- Sussman, R. G., Cohen, B. S., & Lippmann, M. (1991). Asbestos fiber deposition in a human tracheobronchial cast. I. Experimental. *Inhalation Toxicology*, 3, 145–160.
- Tian, L., & Ahmadi, G. (2013). Fiber transport and deposition in human upper tracheobronchial airways. *Journal of Aerosol Science*, 60, 1–20.
- Wang, Z., Hopke, P. K., Ahmadi, G., Cheng, Y.-S., & Baron, P. A. (2008). Fibrous particle deposition in human nasal passage: The influence of particle length, flow rate, and geometry of nasal airway. *Journal of Aerosol Science*, 39, 1040–1054.
- Weibel, E. R. (1963). *Morphometry of the human lung*. New York: Academic Press.
- Yang, X., Liu, Y., & Luo, H. (2006). Respiratory flow in obstructed airways. *Journal of Biomechanics*, 39, 2743–2751.
- Zhang, Z., Kleinstreuer, C., & Kim, C. (2001). Flow structure and particle transport in a triple bifurcation airway model. *Journal of Fluids Engineering*, 123, 320–330.
- Zhang, Z., Kleinstreuer, C., & Kim, C. (2002). Gas–solid two-phase flow in a triple bifurcation lung airway model. *International Journal of Multiphase Flow*, 28, 1021–1046.
- Zhou, Y., Su, W. C., & Cheng, Y. S. (2007). Fiber deposition in the tracheobronchial region: Experimental measurements. *Inhalation Toxicology*, 19, 1071–1078.